Site occupancies in a chemically complex σ-phase from the high-entropy Cr–Mn–Fe–Co–Ni system

Jean-Marc Joubert[1], Yordan Kalchev[2], Andrea Fantin[3,4], Jean-Claude Crivello[1], Rico Zehl[2], Erik Elkaïm[5], Guillaume Laplanche[2]

[1] Univ Paris Est Creteil, CNRS, ICMPE, UMR 7182, 2 rue Henri Dunant, 94320 Thiais, France
[2] Ruhr-Universität Bochum, Universitätsstrasse 150, 44780 Bochum, Germany
[3] Technische Universität Berlin, Hardenbergstr. 36, 10623 Berlin, Germany
[4] Helmholtz-Zentrum Berlin für Materialien und Energie, Hahn-Meitner-Platz 1, 14109 Berlin, Germany
[5] Synchrotron SOLEIL, L'Orme des Merisiers, 91192 Gif-sur-Yvette, France

Supplementary Material

The present supplementary document provides additional details concerning:

Specimen preparation

From the homogenized button of the quinary σ-phase, 4-mm thick slices were cut at various locations by electrical discharge machining (EDM). These slices showed a large density of cracks that were formed during cooling after melting, homogenization of the alloy or EDM cutting. As a next step, each slice was ground with SiC papers to a grit size of 2500 and then electropolished at 40 V for 10 s using an A2 "Struers" electrolyte consisting of 70 vol.% ethanol, 12 vol.% distilled water, 10 vol.% diethylene glycol monobuthylethene, and 8 vol.% (70-72%) perchloric acid.

Using the electropolished slices, the chemical homogeneity and microstructure of the quinary σ phase were investigated. Its chemical composition was measured by energy-dispersive X-ray spectroscopy (EDX) in a JEOL JSM-7200F FE-scanning electron microscope (SEM) equipped with an Oxford X-Max 80 SDD EDX spectrometer. In addition, electron backscatter diffraction (EBSD) experiments were also carried out in the same apparatus for microstructure and phase analyses. The latter was further complemented by X-ray diffraction (XRD). For this purpose, the brittle σ-phase button was manually milled in a mortar until a fine powder was obtained. The XRD analysis was then performed on a Bruker D8 Advance working with Cu Kα radiation and equipped with a graphite monochromator in the diffracted beam.

Characterization of the samples

A BSE micrograph, EBSD phase map, and grain orientation map, as well as a representative Kikuchi pattern are displayed in Fig. S2. These images reveal that the quinary alloy is mostly single phase (>99% σ phase), i.e., the pixels of the phase map in Fig. S2b appear yellow when the corresponding Kikuchi patterns (e.g., Fig. S2d) were indexed with the crystallographic structure of the σ phase. The quinary alloy exhibits a coarse-grained microstructure, for instance only two grains with red and pink colors are visible in the grain orientation map, Fig. S2c. The white arrows in Fig. S2a mark large cracks, which reflect the high brittleness of the σ phase while the black dots were either identified by EDX as small pores or Cr-rich oxides. In a previous study, we also showed that the alloy contains a small amount of a secondary *fcc* phase as shown in Fig. 4 of Ref. [1]. The presence of very small amounts of spinel (oxide) and *fcc* phases was further confirmed by XRD and these phases were considered in the Rietveld refinement of the resonant X-ray data. The composition of the quinary σ phase was determined by EDX point analyses at five distinct positions. The values were not found to significantly differ, indicating that the alloy is chemically homogeneous and the average value was $Cr_{47.4}Mn_{14.5}Fe_{16.2}Co_{16.7}Ni_{5.3}$ (in at.%), which is close to the nominal alloy composition ($Cr_{46}Mn_{15.2}Fe_{16.3}Co_{17}Ni_{5.5}$).

The standard binary $Mn_{60}Co_{40}$ alloy is single phase with a measured composition very close to the nominal one ($Mn_{59.9(1)}Co_{40.1(1)}$). It is a substitutional solid solution based on β-Mn. The structure is cubic with a lattice parameter a = 6.284 Å [2]. The sample was measured with neutron diffraction

allowing the determination of the site occupancies of the two atoms on the two sites of the crystal structure (8*c*: 6.33 Co/1.67 Mn; 12*d*: 1.69 Co/10.31 Mn) [2].

XANES at SOLEIL and EXAFS measurements at ESRF

Conditions for the measurements at Soleil and at the ESRF are given in Tables S2 and S3, respectively. Specimens were prepared from the same powder used in the anomalous diffraction experiment. It was mixed with cellulose to obtain a pellet, with a diameter of 1.3 cm, for which the total absorption in transmission is kept below 1.5 absorption units above the edges.

Standard procedures [3] were followed to extract the structural EXAFS signal (k*$\chi(k)$): pre-edge background removal, spline modeling of bare atomic background, post-edge normalization (polynomial functions) and energy calibration using the software ATHENA [4]. Models of atomic clusters centered on each absorber atom were obtained by ATOMS [5], while amplitudes and phase functions were calculated using the FEFF8 code [6]. EXAFS spectra were finally fit through the ARTEMIS software [4] in the Fourier-Transform (FT) space.

Figures

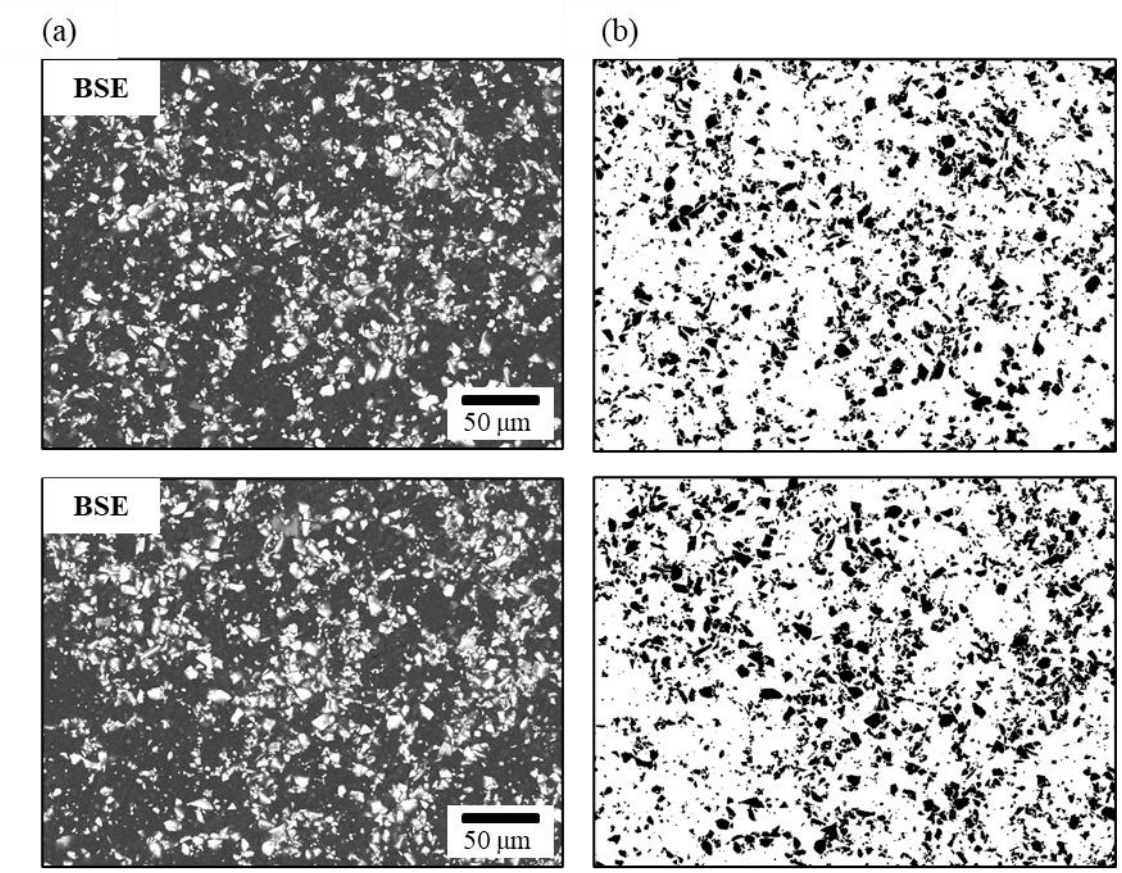

Fig. S1. SEM micrographs of the sieved and embedded quinary σ-phase powder with a particle size lower than 10 µm. (a) Representative BSE image showing bright powder particles on a dark background (corresponding to epoxy). The BSE image shown in (a) was binarized and the result is shown in (b). Here, the powder particles are black on a white background.

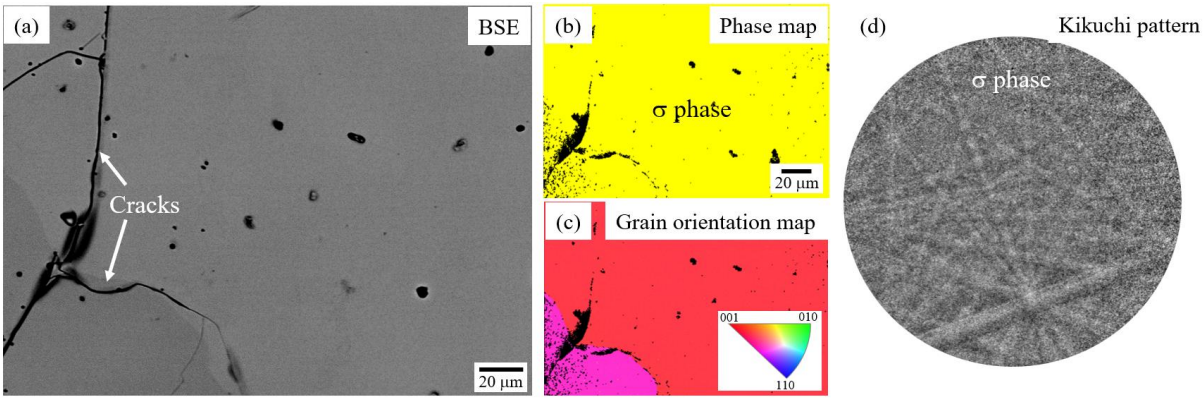

Fig. S2. Microstructure of the quinary σ phase. (a) BSE micrograph showing cracks highlighted with white arrows. The dark dots are either small pores or oxides. (b) EBSD phase map showing that the alloy is single phase (σ phase in yellow). (c) Grain orientation map. (d) Representative Kikuchi pattern.

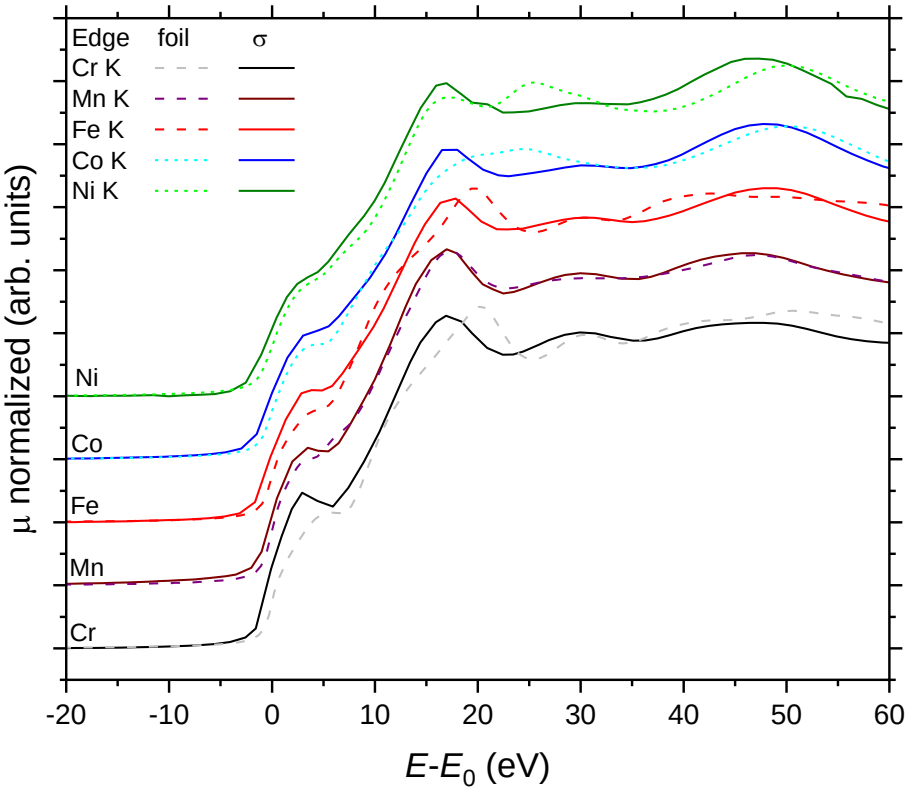

Fig. S3. XANES region for each K-edge spectrum of the quinary σ phase, superimposed with the corresponding reference foil (of pure metals) and plotted as a function of E-E_0 (eV) (ESRF measurement, with E_0 the energy at the inflection point of the corresponding foil).

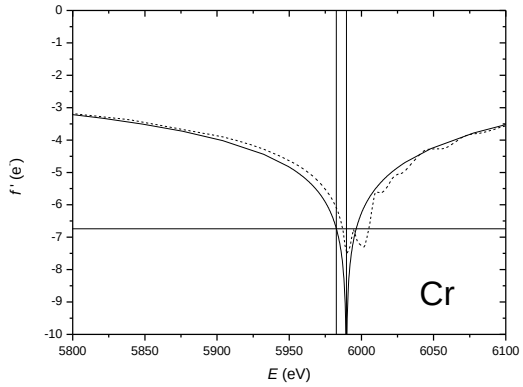
f ' (e)
E (eV)
Cr

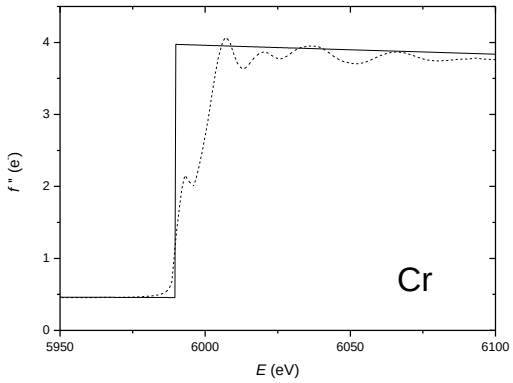
f '' (e)
E (eV)
Cr

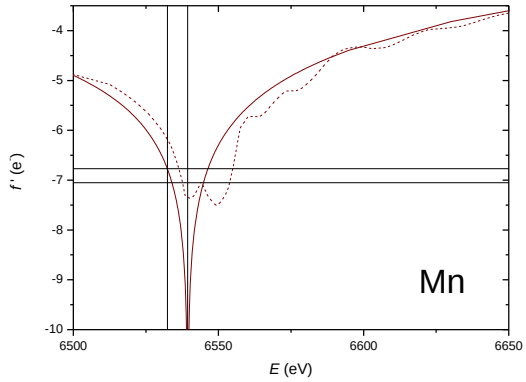
f ' (e)
E (eV)
Mn

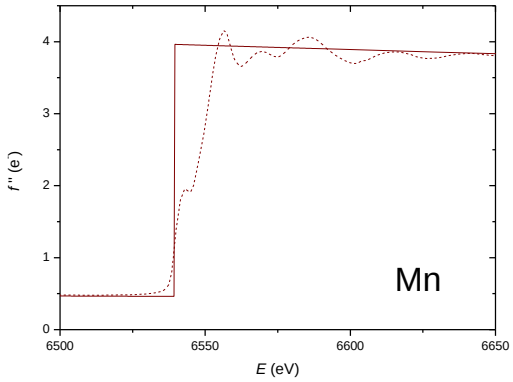
f '' (e)
E (eV)
Mn

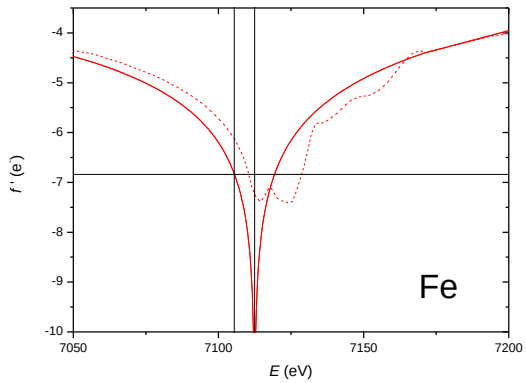
f ' (e)
E (eV)
Fe

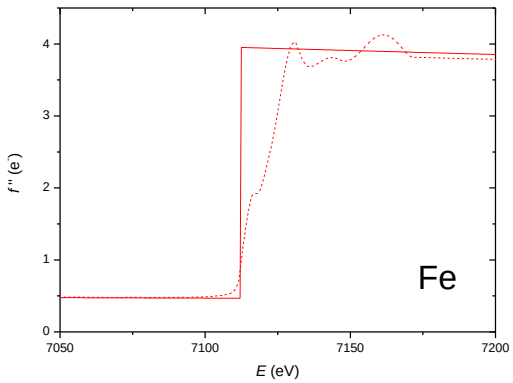
f '' (e)
E (eV)
Fe

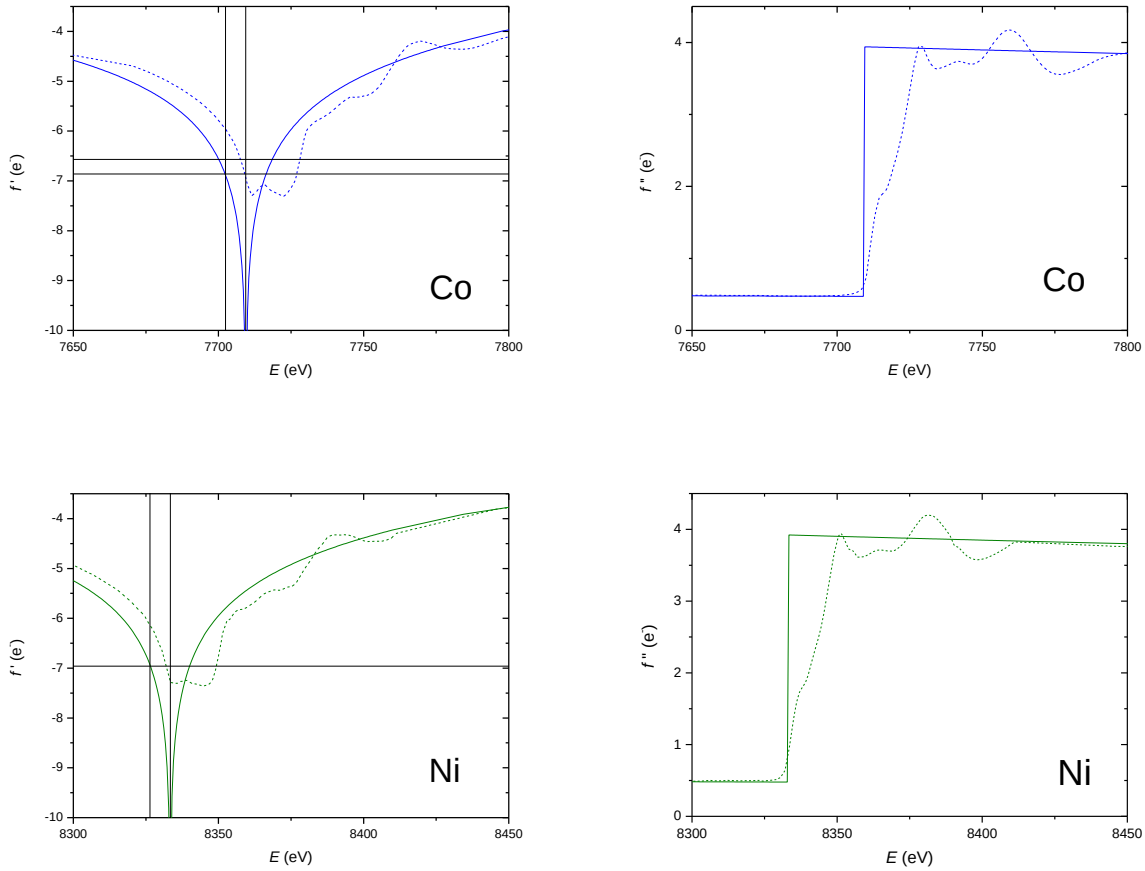

Fig. S4. Dispersion coefficients *f'* (left column) and *f''* (right) at the different edges as a function of X-ray energy. Sasaki (full lines) and KKR (dashed lines) values are shown. Vertical lines indicate Sasaki's edge and the measurement done at -7 eV. Horizontal lines show the Sakaki values for *f'* at 7 eV below the edge. For Mn and Co, the *f''* values obtained from the reference samples are also shown.

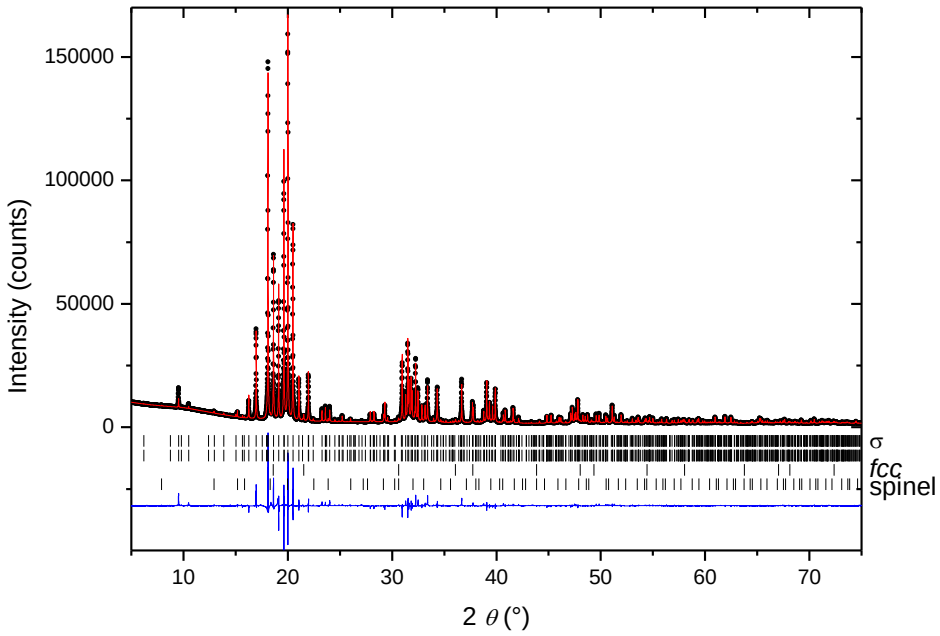

Fig. S5. Rietveld analysis of the XRD pattern of the quinary σ phase at **18469 eV**. Experimental (points), calculated (red line) and difference (blue line below) patterns are shown. The markers from top to bottom show the positions of the σ phase (duplicated), *fcc*, spinel and β-MnNi.

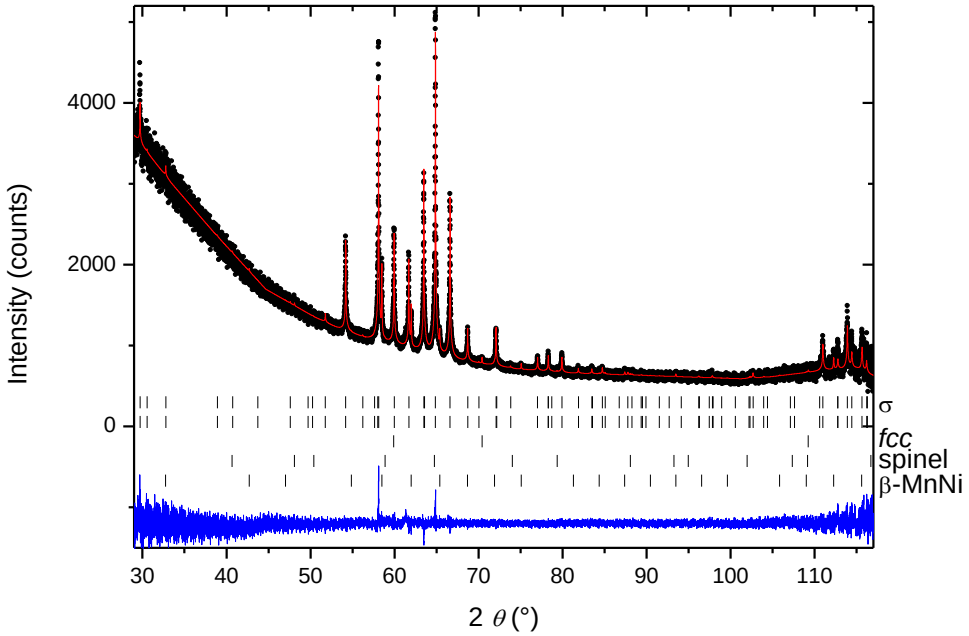

Fig. S6. Rietveld analysis of the XRD pattern of the quinary σ phase at **5982 eV (7 eV below the Cr edge)**. Experimental (points), calculated (red line) and difference (blue line below) patterns are

shown. The markers from top to bottom show the positions of the σ phase (duplicated), *fcc*, spinel and β-MnNi.

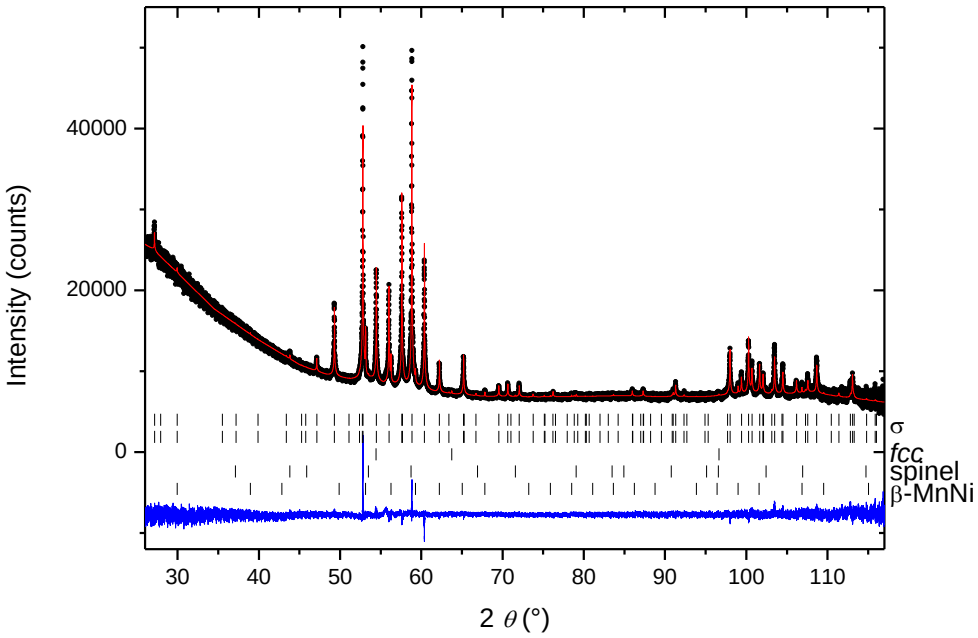

Fig. S7. Rietveld analysis of the XRD pattern of the quinary σ phase at **6531 eV (7 eV below the Mn edge)**. Experimental (points), calculated (red line) and difference (blue line below) patterns are shown. The markers from top to bottom show the positions of the σ phase (duplicated), *fcc*, spinel and β-MnNi.

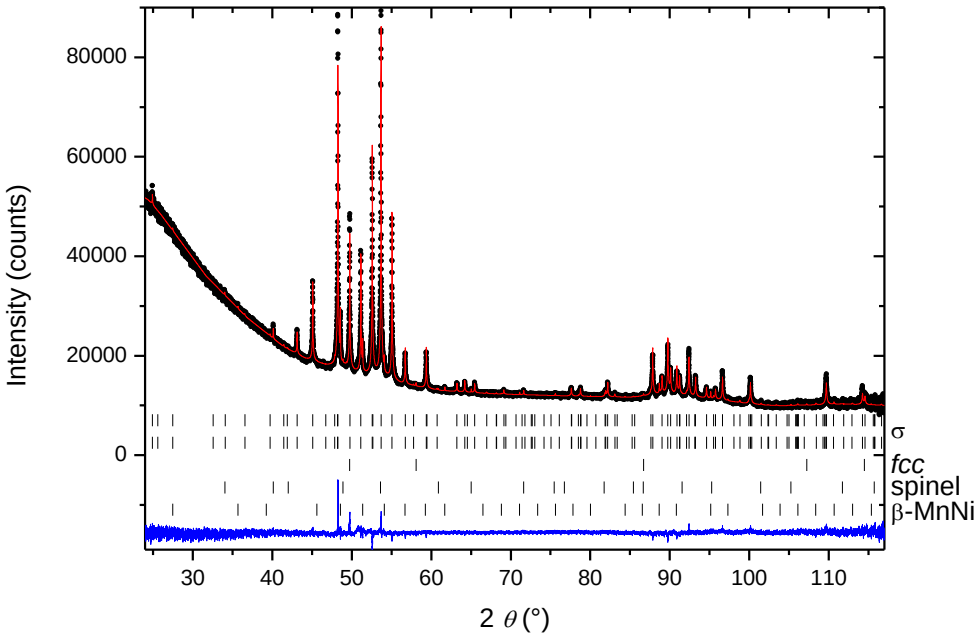

Fig. S8. Rietveld analysis of the XRD pattern of the quinary σ phase at **7104 eV (7 eV below the Fe edge)**. Experimental (points), calculated (red line) and difference (blue line below) patterns are shown. The markers from top to bottom show the positions of the σ phase (duplicated), *fcc*, spinel and β-MnNi.

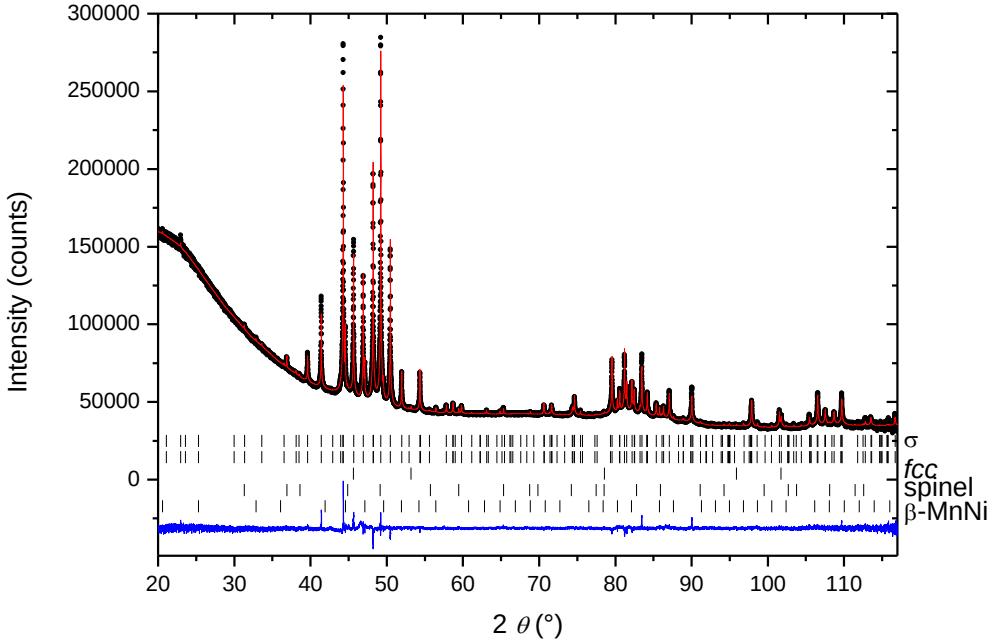

Fig. S9. Rietveld analysis of the XRD pattern of the quinary σ sample at 7702 eV **(7 eV below the Co edge)**. Experimental (points), calculated (red line) and difference (blue line below) patterns are shown. The markers from top to bottom show the positions of the σ phase (duplicated), *fcc*, spinel and β-MnNi.

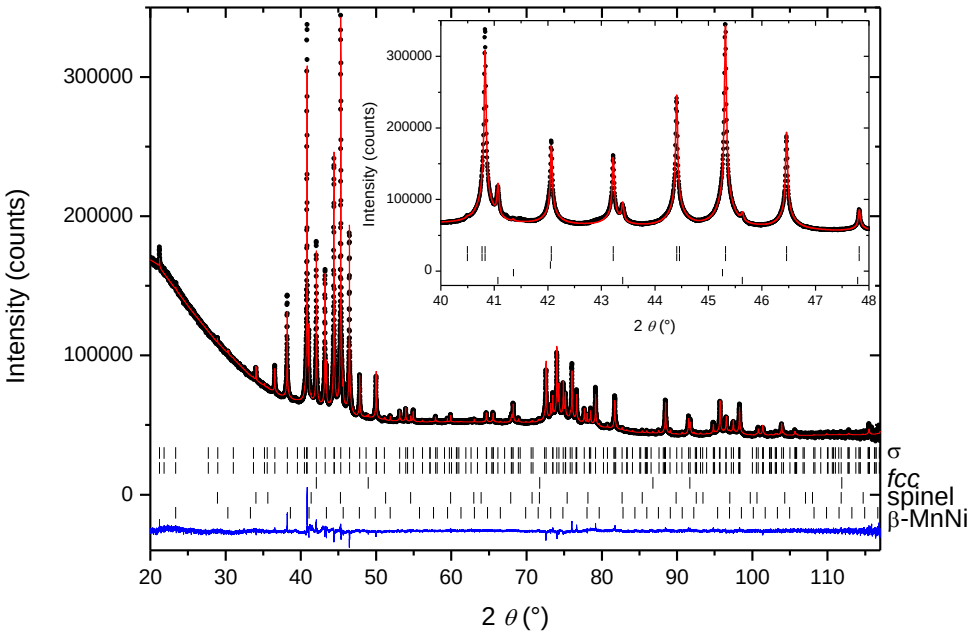

Fig. S10. Rietveld analysis of the XRD pattern of the quinary σ sample at **8325 eV (7 eV below the Ni edge)**. Experimental (points), calculated (red line) and difference (blue line below) patterns are shown. The markers from top to bottom show the positions of the σ phase (duplicated), *fcc*, spinel and β-MnNi.

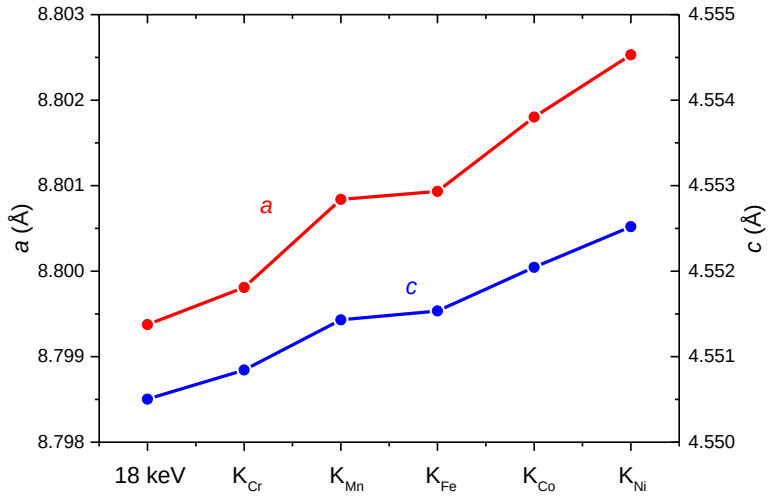

Fig. S11. Lattice parameters of the σ phase refined for the different diffraction patterns.

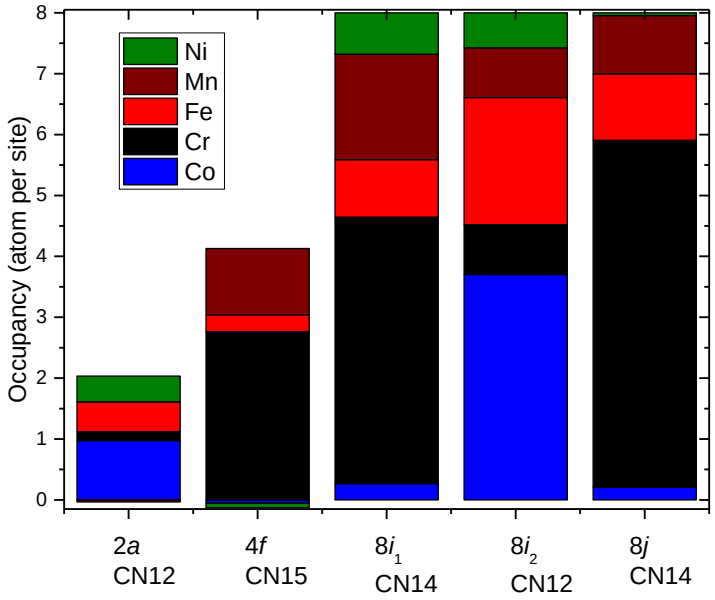

Fig. S12. Site occupancies of Cr, Mn, Fe, Co, and Ni on the five different sublattices of the quinary σ phase obtained experimentally from resonant diffraction experiment (*f'* values from KKR).

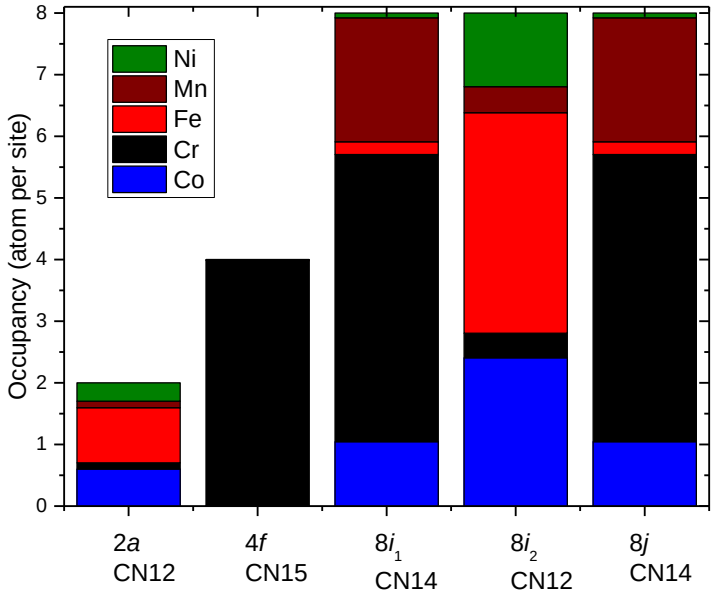

Fig. S13. Site occupancies of the quinary σ phase calculated at 1000 K with TCHEA4 database.

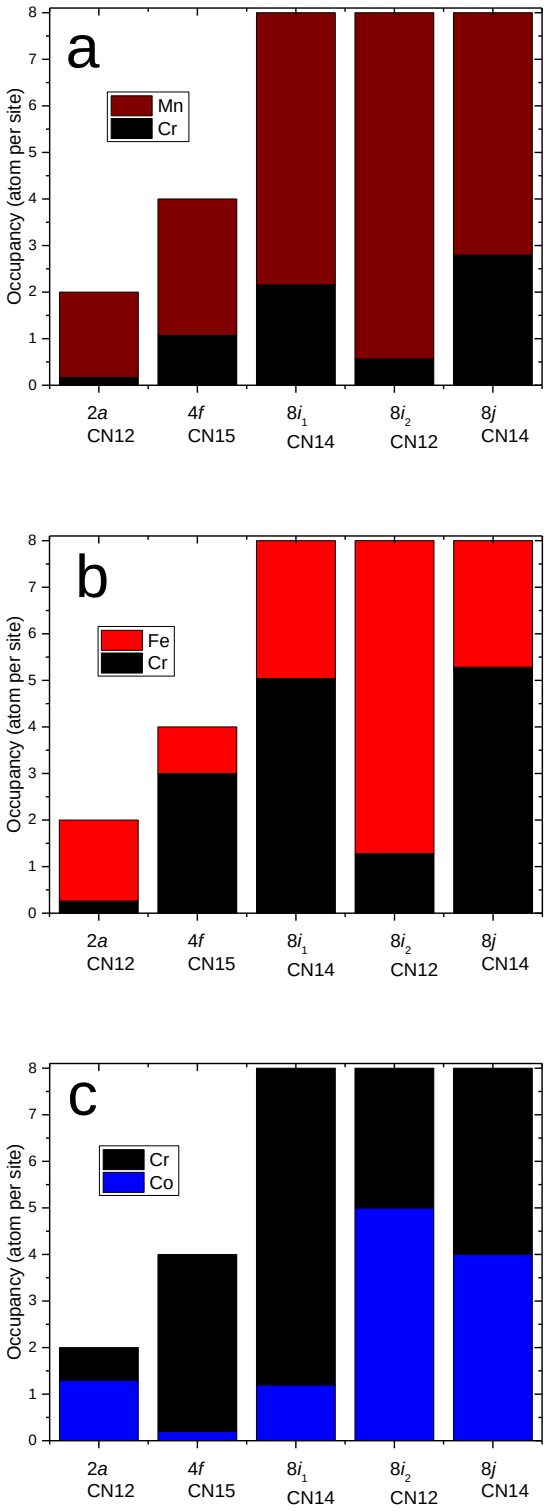

Fig. S14. Site occupancies in the binary σ phases $Cr_{22.5}Mn_{77.5}$ [7] (a), $Cr_{49.5}Fe_{50.5}$ [8] (b) and $Cr_{61}Co_{39}$ [9] (c).

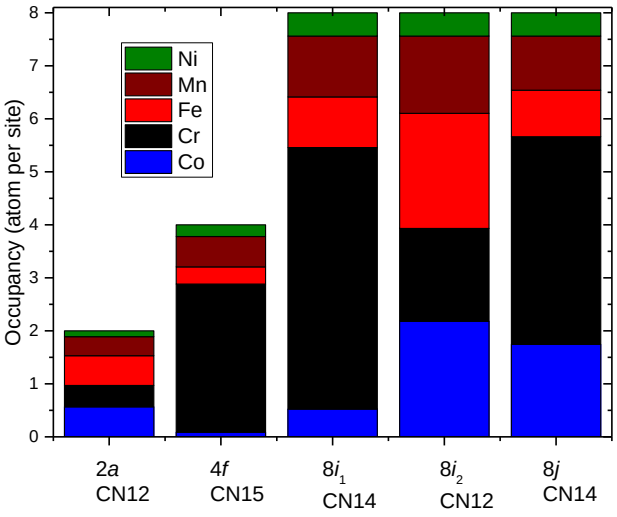

Fig. S15. Site occupancies of the quinary σ phase predicted from the experimental binary results of $Cr_{22.5}Mn_{77.5}$ [7], $Cr_{49.5}Fe_{50.5}$ [8] and $Cr_{61}Co_{39}$ [9] with the following assumptions: the distribution of Mn, Fe and Co is calculated from the binary systems proportionally to the composition in the quinary system, Ni for which no information is available is distributed statistically, Cr complements up to full occupancy of each site.

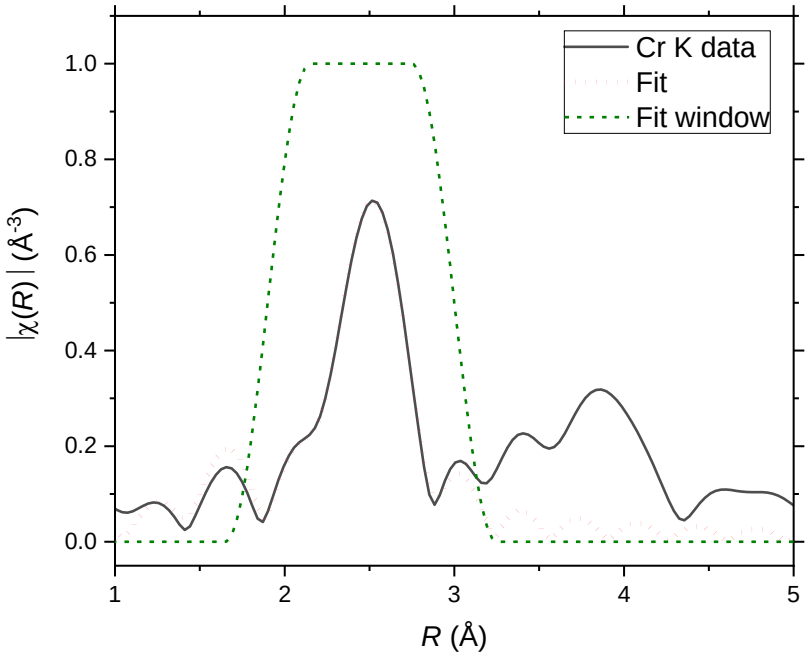
Cr K data
Fit
Fit window
1.0
0.8
0.6
0.4
0.2
0.0
|χ(R)| (Å-3)
1
2
3
4
5
R (Å)

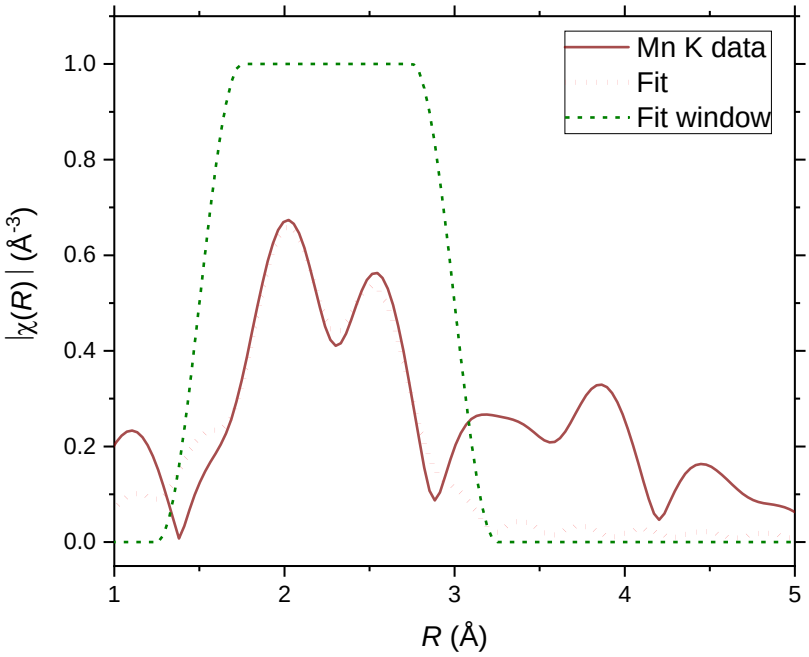
Mn K data
Fit
Fit window
1.0
0.8
0.6
0.4
0.2
0.0
|χ(R)| (Å-3)
1
2
3
4
5
R (Å)

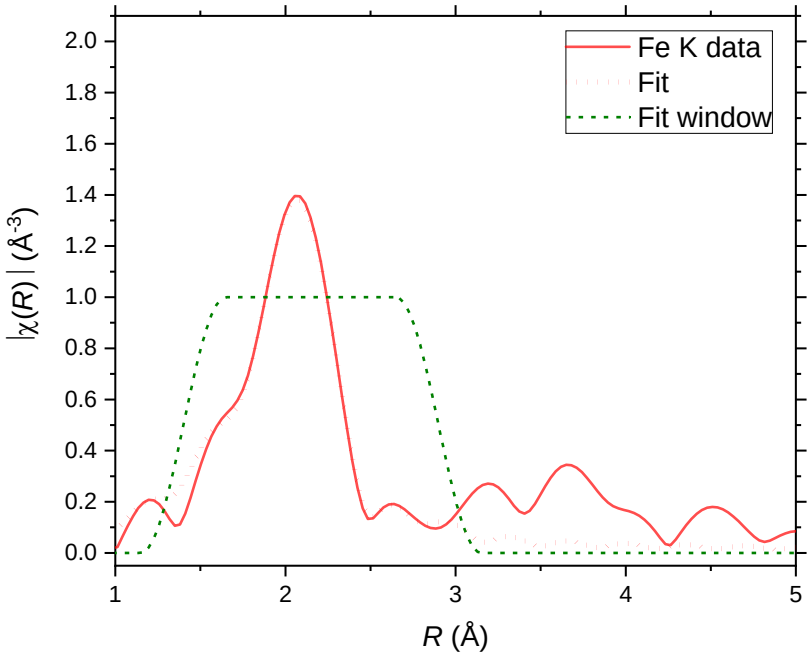
Fe K data
Fit
Fit window
|χ(R)| (Å-3)
R (Å)
0.0
0.2
0.4
0.6
0.8
1.0
1.2
1.4
1.6
1.8
2.0
1
2
3
4
5

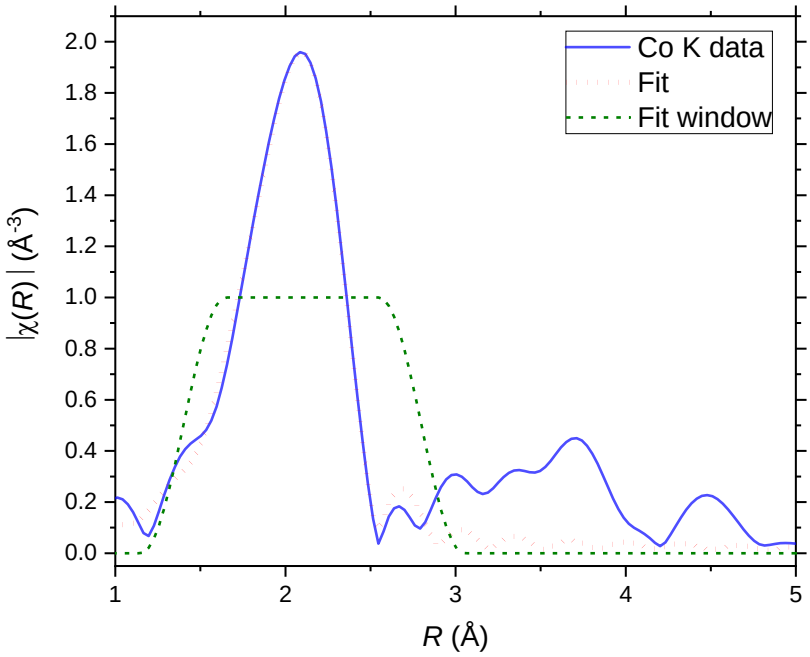
Co K data
Fit
Fit window
|χ(R)| (Å-3)
R (Å)
0.0
0.2
0.4
0.6
0.8
1.0
1.2
1.4
1.6
1.8
2.0
1
2
3
4
5

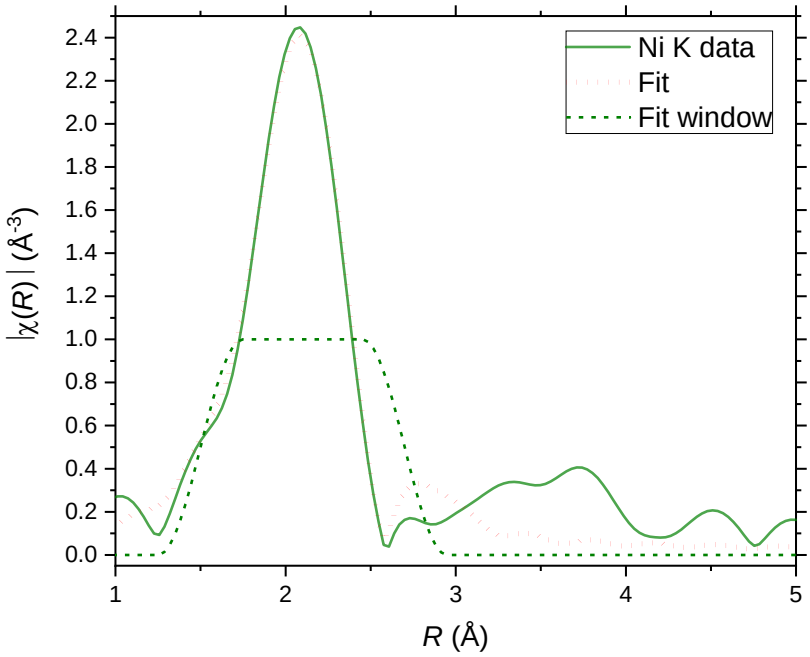

Fig. S16. First shell EXAFS refinements using the relative occupancies reported in Table 1. Data (Cr: black, Mn: brown, Fe: red, Co: blue, and Ni: green solid lines) and fit (dotted red lines) in the corresponding window (green dashed lines); 30% transparency was applied to K-edge data for better visualization. Fitting in R space is used and plots are not phase corrected.

Tables

Table S1: Environment around each site in the crystal structure of the σ phase.

Wyckoff position	Environment	Distance (diffraction) (Å)
2*a*	4*f*	2.602
CN12	4*f*	2.602
	4*f*	2.602
	4*f*	2.602
	$8i_2$	2.357
	$8i_2$	2.357
	$8i_2$	2.357
	$8i_2$	2.357
	8*j*	2.539
	8*j*	2.539
	8*j*	2.539
	8*j*	2.539
4*f*	2*a*	2.602
CN15	2*a*	2.602
	4*f*	2.508
	$8i_1$	2.431
	$8i_1$	2.431
	$8i_2$	2.685
	$8i_2$	2.685
	$8i_2$	2.685
	$8i_2$	2.685
	8*j*	2.930
	8*j*	2.830
	8*j*	2.830
	8*j*	2.830
	8*j*	2.930
	8*j*	2.830
$8i_1$	4*f*	2.431
CN14	$8i_1$	2.831
	$8i_1$	2.831
	$8i_1$	2.382
	$8i_1$	2.831
	$8i_1$	2.831
	$8i_2$	2.491
	$8i_2$	2.490
	$8i_2$	2.490
	$8i_2$	2.500
	8*j*	2.771
	8*j*	2.769
	8*j*	2.769
	8*j*	2.771

8i_2	2a	2.357
CN12	4f	2.692
	4f	2.692
	8i_1	2.490
	8i_1	2.500
	8i_1	2.490
	8i_1	2.490
	8i_2	2.407
	8j	2.559
	8j	2.539
	8j	2.559
	8j	2.539
8j	2a	2.539
CN14	4f	2.930
	4f	2.830
	4f	2.830
	8i_1	2.771
	8i_1	2.769
	8i_1	2.771
	8i_1	2.769
	8i_2	2.539
	8i_2	2.559
	8i_2	2.539
	8i_2	2.559
	8j	2.285
	8j	2.276

Table S2: Edge type, corresponding edge energies (foil and σ phase) at CRISTAL beamline, SOLEIL.

Edge	Edge foil E_0 (eV)	Edge σ E_0 (eV)
Cr K	5989.2	5988.7
Mn K	6539	6538.8
Fe K	7112	7112.3
Co K	7708.9	7709.4
Ni K	8332.8	8332.9

Table S3: Edge type, corresponding edge energies (foil and σ phase) and measured k_{max} at BM-08, ESRF.

Edge	Edge foil E_0 (eV)	k_{max} (Å^{-1})	Edge σ E_0 (eV)	k_{max} (Å^{-1})
Cr K	5989.2	18	5989.2	11.8
Mn K	6539	18	6539.5	12.0
Fe K	7112	18	7112.6	12.2
Co K	7708.9	18	7709.7	12.4
Ni K	8332.8	18	8333.7	15

Table S4: Dispersion coefficient f' for the anomalous scatterer obtained from the Sasaki's tables, KKR and the refinement of a reference sample.

Resonant element	Energy (eV)	Distance to the edge (eV)	f' from Sasaki (e^-)	f' from KKR (e^-)	f' from reference (e^-)
Cr	5982.58	-7	-6.74	-6.03	
Mn	6532.4	-7	-6.77	-6.14	-7.05
Fe	7105.46	-7	-6.84	-6.12	
Co	7702.4	-7	-6.86	-5.96	-6.57
Ni	8326.4	-7	-6.96	-6.10	

Table S5: List of the measured samples. The quantity of sample (mixed with capillary powder) is indicated with the capillary diameter in mm.

Sample	18 keV	Mn edge	Co edge	Cr, Fe and Ni edges
Silicon	50% 0.3	50% 0.3		50% 0.3
σ	100% 0.3	50% 0.2		50% 0.2
β-MnCo		100% 0.2	25% 0.2	

Table S6: Site occupancies (estimated standard deviation: 0.1 atom) obtained from the joint refinement of the five resonant diffraction data using the dispersion coefficients from Sasaki and from KKR, and from the calculation based on the combined machine learning-DFT thermodynamic model.

		occupancies in atoms				
Technique	site (CN)	Cr	Mn	Fe	Co	Ni
refinement	2*a* (12)	0.23	-0.01	0.48	0.88	0.42
(Sasaki)	4*f* (15)	2.65	1.05	0.31	0.05	-0.06
	$8i_1$ (14)	4.34	1.67	0.97	0.44	0.57
	$8i_2$ (12)	1.13	0.81	2.03	3.34	0.69
	8*j* (14)	5.45	1.04	1.09	0.39	0.03
refinement	2*a* (12)	0.15	-0.03	0.49	0.97	0.42
(KKR)	4*f* (15)	2.76	1.09	0.28	-0.05	-0.07
	$8i_1$ (14)	4.38	1.73	0.94	0.27	0.68
	$8i_2$ (12)	0.82	0.82	2.09	3.7	0.57
	8*j* (14)	5.7	0.96	1.09	0.21	0.04
ML-DFT	2*a* (12)	0.12	0.46	1.04	0.22	0.16
	4*f* (15)	3.06	0.55	0.19	0.11	0.09
	$8i_1$ (14)	4.7	1.42	0.7	0.73	0.44
	$8i_2$ (12)	0.2	1.03	2.6	3.54	0.64
	8*j* (14)	5.72	1.11	0.35	0.49	0.33

Table S7: EXAFS fits results based on the diffraction model for each Wyckoff site and each edge, where distances in Å (d_i(Å) for each *i*) are reported together with their fit uncertainty (Δ(Å)) and compared to those obtained by diffraction; results are depicted in Fig. 8.

2*a*	d1(Å)	Δ(Å)	d2(Å)	Δ(Å)	d3(Å)	Δ(Å)
Fe	2.448	0.08	2.634	0.09	2.695	0.09
Co	2.336	0.038	2.514	0.04	2.572	0.042
Ni	2.414	0.069	2.599	0.073	2.658	0.076
Diffr	2.357	0.004	2.539	0.003	2.602	0.002

4*f*	d1(Å)	Δ(Å)	d2(Å)	Δ(Å)	d3(Å)	Δ(Å)	d4(Å)	Δ(Å)	d5(Å)	Δ(Å)	d6(Å)	d1(Å)
Cr	2.545	0.022	2.624	0.024	2.722	0.025	2.817	0.026	2.962	0.027	3.067	0.028
Mn	2.413	0.06	2.514	0.063	2.597	0.066	2.685	0.068	2.826	0.07	2.913	0.07
Fe	2.453	0.22	2.556	0.22	2.64	0.22	2.729	0.23	2.872	0.25	2.961	0.25
Diffr	2.431	0.005	2.508	0.005	2.602	0.002	2.692	0.003	2.83	0.004	2.93	0.004

8*i*1	d1(Å)	Δ(Å)	d2(Å)	Δ(Å)	d3(Å)	Δ(Å)	d4(Å)	Δ(Å)	d5(Å)	Δ(Å)	d6(Å)	Δ (Å)	d7(Å)	Δ(Å)	d8(Å)	Δ(Å)
Cr	2.362	0.005	2.411	0.006			2.472	0.006			2.727	0.007			2.811	0.007
Mn	2.402	0.012	2.481	0.013			2.759	0.013			2.833	0.014				
Fe	2.415	0.04	2.439	0.04			2.506	0.04			2.787	0.050			2.862	0.05
Co	2.387	0.047	2.411	0.049			2.447	0.051			2.754	0.053			2.829	0.055
Ni	2.425	0.033	2.449	0.034			2.517	0.036			2.799	0.038			2.874	0.04
Diffr	2.382	0.005	2.431	0.005	2.490	0.002	2.491	0.005	2.500	0.005	2.771	0.004	2.835	0.003	2.831	0.003

8*i*2	d1(Å)	Δ(Å)	d2(Å)	Δ(Å)	d3(Å)	Δ(Å)	d4(Å)	Δ(Å)	d5(Å)	Δ(Å)	d6(Å)	Δ(Å)	d7(Å)	Δ(Å)
Cr	2.41	0.019	2.462	0.02			2.547	0.021	2.547	0.021	2.605	0.021	2.751	0.022
Mn	2.381	0.026	2.436	0.027			2.503	0.028	2.548	0.029	2.581	0.03	2.711	0.031
Fe	2.335	0.015	2.389	0.015			2.455	0.015	2.499	0.015	2.532	0.016	2.658	0.016
Co	2.332	0.009	2.386	0.009			2.452	0.01	2.496	0.01	2.529	0.011	2.655	0.011
Ni	2.365	0.033	2.419	0.034			2.486	0.035	2.531	0.036	2.564	0.036	2.692	0.037
Diffr	2.357	0.004	2.407	0.005	2.490	0.002	2.500	0.005	2.539	0.005	2.559	0.004	2.692	0.003

8*j*	d1(Å)	Δ(Å)	d2(Å)	Δ(Å)	d3(Å)	Δ(Å)	d4(Å)	Δ(Å)	d5(Å)	Δ(Å)	d6(Å)	Δ (Å)	d7(Å)	Δ(Å)	d8(Å)	Δ(Å)
Cr	2.298	0.005	2.568	0.006	2.793	0.006	2.853	0.007	2.954	0.007						
Mn	2.213	0.03	2.249	0.03	2.483	0.032	2.511	0.034	2.708	0.036	2.774	0.038	2.861	0.04		
Fe	2.204	0.035	2.24	0.035	2.473	0.035	2.5	0.036	2.696	0.036	2.763	0.037	2.849	0.038		
Co	2.24	0.1	2.277	0.1	2.514	0.1	2.542	0.1	2.741	0.1	2.808	0.11	2.896	0.11		
Diffr	2.276	0.008	2.285	0.008	2.539	0.004	2.559	0.004	2.769	0.004	2.771	0.004	2.83	0.004	2.93	0.004

References

[1] J. Zhang, G.M. Muralikrishna, A. Asabre, Y. Kalchev, J. Müller, B. Butz, S. Hilke, H. Rösner, G. Laplanche, S.V. Divinski, G. Wilde, Tracer diffusion in the σ phase of the CoCrFeMnNi system, Acta Mater. 203 (2021) 116498.
[2] J.-M. Joubert, J.-C. Crivello, Crystallographic study of β-Mn solid solutions, to be published.
[3] P.A. Lee, P.H. Citrin, P. Eisenberger, B.M. Kincaid, Extended X-ray absorption fine structure - its strengths and limitations as a structural tool, Review of Modern Physics 53 (1981) 769.
[4] B. Ravel, M. Newville, ATHENA and ARTEMIS: interactive graphical data analysis using IFEFFIT, Physica Scripta T115 (2005) 1007-1010.
[5] B. Ravel, ATOMS: crystallography for the X-ray absorption spectroscopist, J. Synchrotron Radiat. 8 (2001) 314-316.
[6] A.L. Ankudinov, B. Ravel, J.J. Rehr, S.D. Conradson, Real-space multiple-scattering calculation an dinterpretation of X-ray absorption near-edge structure, Phys. Rev. B58 (1998) 7565.
[7] J.-M. Joubert, Intermetallic compounds of the Cr-Mn system investigated using *in situ* powder neutron diffraction: the reported order-disorder transformation of the σ phase elucidated, Intermetallics 146 (2022) 107580.
[8] H.L. Yakel, Atom distribution in sigma phases. I. Fe and Cr atom distribution in a binary sigma phase equilibrated at 1063, 1013 and 923 K, Acta Crystallogr. B39 (1983) 20-28.
[9] S.H. Algie, E.O. Hall, Site ordering in some σ phase structures, Acta Crystallogr. 20 (1966) 142.